catalysts

MDPI

Article

Nano-Sheets of $CsNiVF_6$ Pyrochlore Electrocatalyst for Enhanced Urea Oxidation and Hydrogen Green Production Reactions

Mohamed A. Ghanem *, Abdullah M. Al-Mayouf, Khalaf A. Alfudhayli and Mohamed O. Abdelkader

Chemistry Department, College of Science, King Saud University, Riyadh 11451, Saudi Arabia; amayouf@ksu.edu.sa (A.M.A.-M.); 442106652@student.ksu.edu.sa (K.A.A.); 439105661@student.ksu.edu.sa (M.O.A.)

* Correspondence: mghanem@ksu.edu.sa; Tel.: +966-011-4670405

Abstract: This study presents the successful synthesis of a cesium–nickel–vanadium fluoride ($CsNiVF_6$) pyrochlore nano-sheet catalyst via solid-phase synthesis and its electrochemical performance in green hydrogen production through urea electrolysis in alkaline media. The physicochemical characterizations revealed that the $CsNiVF_6$ exhibits a pyrochlore-type structure consisting of a disordered cubic corner-shared (Ni, V)F_6 octahedra structure and nano-sheet morphology with a thickness ranging from 10 to 20 nm. Using the $CsNiVF_6$ catalyst, the electrochemical analysis, conducted through cyclic voltammetry, demonstrates a current mass activity of ~1500 mA mg^{-1}, recorded at 1.8 V vs. RHE, along with low-resistance (3.25 ohm) charge transfer and good long-term stability for 0.33 M urea oxidation in an alkaline solution. Moreover, the volumetric hydrogen production rate at the cathode (bare nickel foam) is increased from 12.25 to 39.15 µmol/min upon the addition of 0.33 M urea to a 1.0 KOH solution and at a bias potential of 2.0 V. The addition of urea to the electrolyte solution enhances hydrogen production at the cathode, especially at lower voltages, surpassing the volumes produced in pure 1.0 M KOH solution. This utilization of a $CsNiVF_6$ pyrochlore nano-sheet catalyst and renewable urea as a feedstock contributes to the development of a green and sustainable hydrogen economy. Overall, this research underscores the potential use of $CsNiVF_6$ as a cost-effective nickel-based pyrochlore electrocatalyst for advancing renewable and sustainable urea electrolysis processes toward green hydrogen production.

Keywords: pyrochlore structure; CsNiVF6; hydrogen green production; urea electrolysis

Citation: Ghanem, M.A.; Al-Mayouf, A.M.; Alfudhayli, K.A.; Abdelkader, M.O. Nano-Sheets of $CsNiVF_6$ Pyrochlore Electrocatalyst for Enhanced Urea Oxidation and Hydrogen Green Production Reactions. *Catalysts* **2024**, *14*, 325. https://doi.org/10.3390/catal14050325

Academic Editors: Longcheng Zhang and Qian Liu

Received: 21 April 2024
Revised: 9 May 2024
Accepted: 10 May 2024
Published: 16 May 2024

1. Introduction

The search for cost-effective, highly active catalysts for use in energy conversion technologies remains a significant scientific challenge, particularly in facilitating the key electrochemical reactions of oxygen reduction (ORR) and evolution (OER) in various applications such as metal–air batteries, fuel cells, water electrolysis and direct solar water splitting [1–6]. Hydrogen, heralded as a promising energy source for the future due to its high energy density and environmental friendliness, is garnering considerable attention. However, the primary expense of green hydrogen production comes from its significant electricity usage [7]. Therefore, it is crucial to develop and evaluate the physiochemical properties and screening pathways of effective and stable electrocatalysts to decrease both their electricity usage and manufacturing expenses to meet the target cost of ~1 USD/kg of hydrogen production [7].

The electrolysis of water, powered by renewable energy sources, emerges as a sustainable approach for reducing the cost of green hydrogen production. Current research and development endeavors in electrolysis technologies are primarily focused on enhancing efficiency, reducing energy consumption, augmenting catalyst performance, and optimizing system design. However, a formidable challenge lies in affecting the two half-reactions of the hydrogen and oxygen evolution reactions (HERs and OERs) during electrochemical

water splitting, primarily due to the intrinsic sluggish kinetics of OERs stemming from a complex multistep proton-coupled electron transfer process [6,8–10].

To address this challenge, researchers have explored the oxidation of small organic molecules such as urea or glycerol as sustainable alternatives for green hydrogen production [11–16]. Furthermore, the concurrent purification of urea-rich wastewater presents additional benefits. Notably, urea electrolysis, involving the reaction ($CO(NH_2)_2 + H_2O \rightarrow N_2 + 3H_2 + CO_2$), boasts a thermodynamic standard cell potential of −0.084 V (vs. RHE), significantly lower than that of water electrolysis (1.23 V) [13,17–20]. Hence, urea electrooxidation holds promise for enhancing efficiency and reducing the cost of green hydrogen production through electrolysis. Previous studies have demonstrated the efficiency of nickel-based catalysts in enhancing the kinetics and lowering the onset oxidation potential of UOR [21–24]. However, the sluggish anodic urea oxidation reaction (UOR) poses a significant obstacle to the overall efficiency of urea electrolysis due to its complex oxidation process [25–28]. The reaction mechanism of urea oxidation in nickel-based catalysts proceeds via the electrochemical–chemical (EC) pathway, forming a Ni(II)/Ni(III) redox system with high-valence oxyhydroxide (NiOOH) active sites; this is followed by the chemical oxidation of urea at the anode while hydrogen is produced at the cathode. Nevertheless, the limited electroactivity of the NiOOH film, attributed to its intrinsic low conductivity, necessitates more conductive and efficient electrocatalysts to bolster the intrinsically sluggish anodic UOR and increase the hydrogen production rate at the cathode [29–32].

In this context, transition metal perovskites (ABO_3), owing to their unique composition diversities and chemical and electronic properties, have garnered considerable interest as efficient anodic and low-cost electrocatalysts for enhancing water-splitting reactions and augmenting the cathodic hydrogen generation rate [33–38]. Moreover, their ionic and electronic conductivity can be further enhanced by fully or partially doping B- and/or O-sites with an appropriate cation or anion to improve their catalytic properties [37–40]. In particular, nickel-containing perovskite oxides have been recently investigated for their ability to enhance the UOR and its associated hydrogen production process [27,41–45]. For instance, Galal et al. [43] reported the electrocatalytic activity of urea oxidation with a lanthanum nickel perovskite (La_2NiO_4)/polyaniline composite, achieving a mass activity of 495 A g^{-1} for the urea oxidation reaction under an optimal composition in alkaline media. Furthermore, the amorphous–crystalline structure of $NiMoO_4$ doped with a Ni_3S_2 heterostructure electrode exhibited significant activity toward the UOR and HER, with a specific activity of ±1000 mA/cm^2 at 1.38 and −263 mV (HER), respectively. In a relevant study, Liang et al. [27] synthesized nanosheet arrays of $NiMoO_4$ using a one-pot hydrothermal method, attaining 830 mA mg^{-1} of current mass activity at 1.56 V versus RHE, and achieving 4.2 times higher urea oxidation activity than the pure $Ni(OH)_2$ catalyst. Additionally, Yang et al. [46] optimized the Ni/Mo molar ratio in $NiMoO_4$ nanorods to enhance the UOR activity. Moreover, Mefford et al. [45] reported the production of a nanostructured $LaNiO_3$ perovskite electrocatalyst for enhanced UOR, revealing a high mass activity of approximately 371 mA mg^{-1} and a specific activity of 2.25 A mg^{-1} in an alkaline solution.

Recently, the $AM^{2+}M^{3+}F_6$ mixed-metal fluorides with A = alkali metal, M^{2+} = Mn, Fe, Co, Ni, Cu, M^{3+} = Al, V, Cr, and Fe that adopt pyrochlore and/or perovskite structures have attracted considerable interest as catalysts due to their varied and unique electronic and functional properties [46–48]. In the structure of the mixed-metal fluoride, the fluoride's electron-withdrawing ability induces a strong positive charge at the M^{2+}/M^{3+} active sites, adjusting the electronic valance state and moderating the intermediate and production adsorption energy, which plays a vital role in enhancing the electrochemical catalytic reaction [49,50].

Moreover, Zhang et al. [51] have discussed how the stacking of rock salt and perovskite layers (n) in nickel and an iron Ruddlesden–Popper (RP) electrocatalyst would affect the Ni/Fe–O covalency and enhance the charge transfer and stability towards OER. The optimum activity/stability was achieved when n increased to 3 compared to structures

with n values of 1 and 2. The results demonstrated the tailoring of Ni/Fe-O synergy and covalency in RP-type perovskites via structural dimensionality for the improvement of the OER activity and stability [51]. In addition, Tang et al. [52] developed a composite of Ruddlesden–Popper (RP) and perovskite layers as the anode for an anion exchange membrane electrolyzer cell (AEMEC). A significant and stable water-splitting current density of 2.01 A cm^{-2} at a potential of 2.00 V was achieved. The enhanced cell performance was attributed to the interfacial strong interaction between the (RP)/perovskite phases and the contribution of lattice oxygen in the water oxidation reaction [52].

Within this context, our group demonstrated the structure and electrochemical activity of mixed nickel aluminum fluoride ($KNiAlF_6$) nanosheets for enhancing the oxidation of an alkaline urea solution [53]. The mixed nickel aluminum fluoride catalyst revealed a urea oxidation onset potential of 1.35 V vs. HRE, a reaction activation energy of 4.02 kJ/mol, a Tafel slope of 22 mV/dec, and a mass activity of 395 mA mg^{-1} at 1.65 V. These results demonstrate the potential direct use of nickel-based perovskite structures as highly active and noble-metal-free catalysts in urea fuel cells or green hydrogen production applications.

Building upon these advancements, this work introduces a new cesium–nickel–vanadium fluoride ($CsNiVF_6$) pyrochlore nano-sheet catalyst, synthesized via the solid-state reaction of stoichiometric precursors. The morphology, structure, and composition of the $CsNiVF_6$ were characterized by scanning electron microscopy (SEM), energy-dispersive X-ray spectroscopy (EDX), X-ray diffraction (XRD) and EDX, respectively. The electrocatalytic activity required for the oxidation of urea and the corresponding hydrogen production rate in the alkaline solution were investigated using electrochemical cyclic voltammetry, chronoamperometry, and impedance spectroscopy (EIS) approaches. The results demonstrate that the pyrochlore mixed-fluoride $CsNiVF_6$ electrode exhibits superior electrocatalytic activity compared to the catalysts reported in the literature for urea oxidation, resulting in a higher hydrogen production rate.

2. Results and Discussion

2.1. Structural and Surface Morphology Characterization of the CsNiVF6 Catalyst

Figure 1a presents the powder X-ray diffraction pattern of the as-synthesized pyrochlore $CsNiVF_6$ catalyst. The resulting XRD pattern displayed the main reflections that align with those previously reported in the relevant studies [51], with a cubic lattice parameter of 10.36 Å. The main characteristic peaks occur at the corresponding specific 2θ angles (*hkl*); notably, those of 24.20 (220), 28.58 (011), 29.80 (222), 34.60 (400), 37.88 (331), 42.70 (422), 45.62 (333), and 49.76° (440) confirm the phase composition and pyrochlore crystal structure of the as-synthesized $CsNiVF_6$ catalyst. The XRD analysis reveals the crystal system of the disordered cubic pyrochlore and specific Fd-3m space group (PDF card No (01-072-1578) [46–48], consistent with the reported literature for transition metals with the general formula $AM_x^{2+}M_{2-x}^{3+}F_6$ in the pyrochlore system [47].

According to the disordered pyrochlore cubic structure [54], the $CsNiVF_6$ catalyst consists of mixed valent $Ni^{2+}/V^{3+}F_6$ corner-sharing octahedra with channels filled with Cs cations, as shown in Figure 1b. Additionally, in the X-ray pattern, a few minor undefined diffraction peaks can be attributed to the residual impurities originating from the starting fluoride precursors, which can be effectively removed by washing with deionized water.

The surface morphology characterization of the $CsNiVF_6$ catalyst at different magnifications is depicted in Figure 2. The low-magnification SEM image (1500X) in Figure 2a reveals a highly porous chunk of microparticles, while the high-magnification images (Figure 2b,c) display unique irregular nanosheet architectures. A detailed analysis of the nanostructures reveals that the nanosheets possess an approximate average thickness ranging from 10 to 20 nm (Figure 2d). The irregular morphology and the presence of nanosheet architectures are critical factors influencing the catalyst's surface properties and, consequently, its catalytic performance.

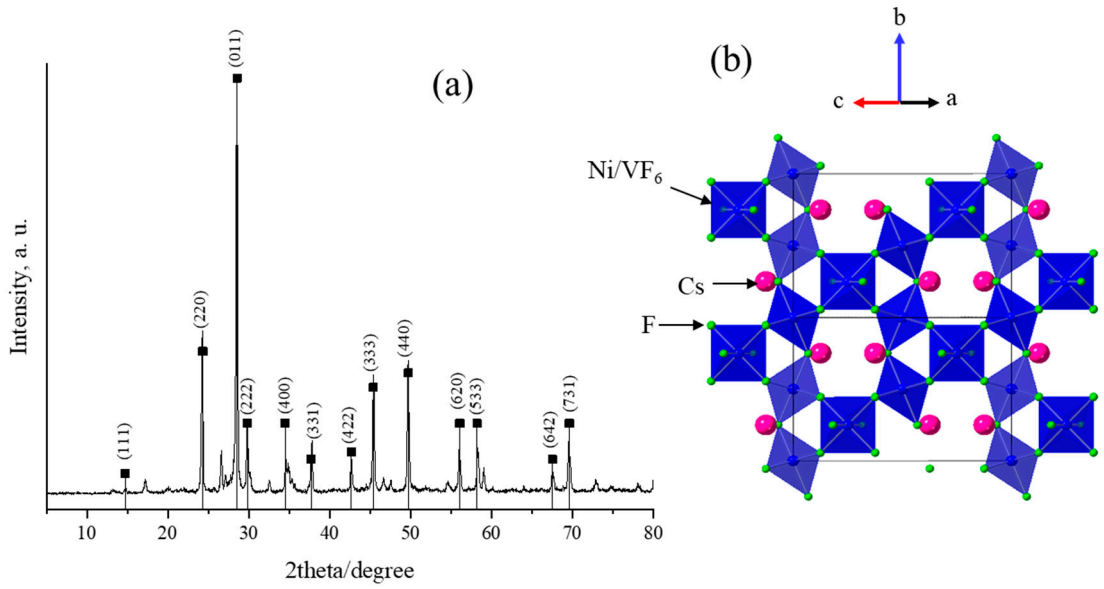

Figure 1. (**a**) X-ray diffraction (PXRD) patterns obtained for the as-prepared $CsNiVF_6$ powder catalyst, and (**b**) the pyrochlore structure of the $CsNiVF_6$ catalyst with the (Ni, V)F_6 octahedra (shaded blue), fluoride (green) and Cs ions (magenta).

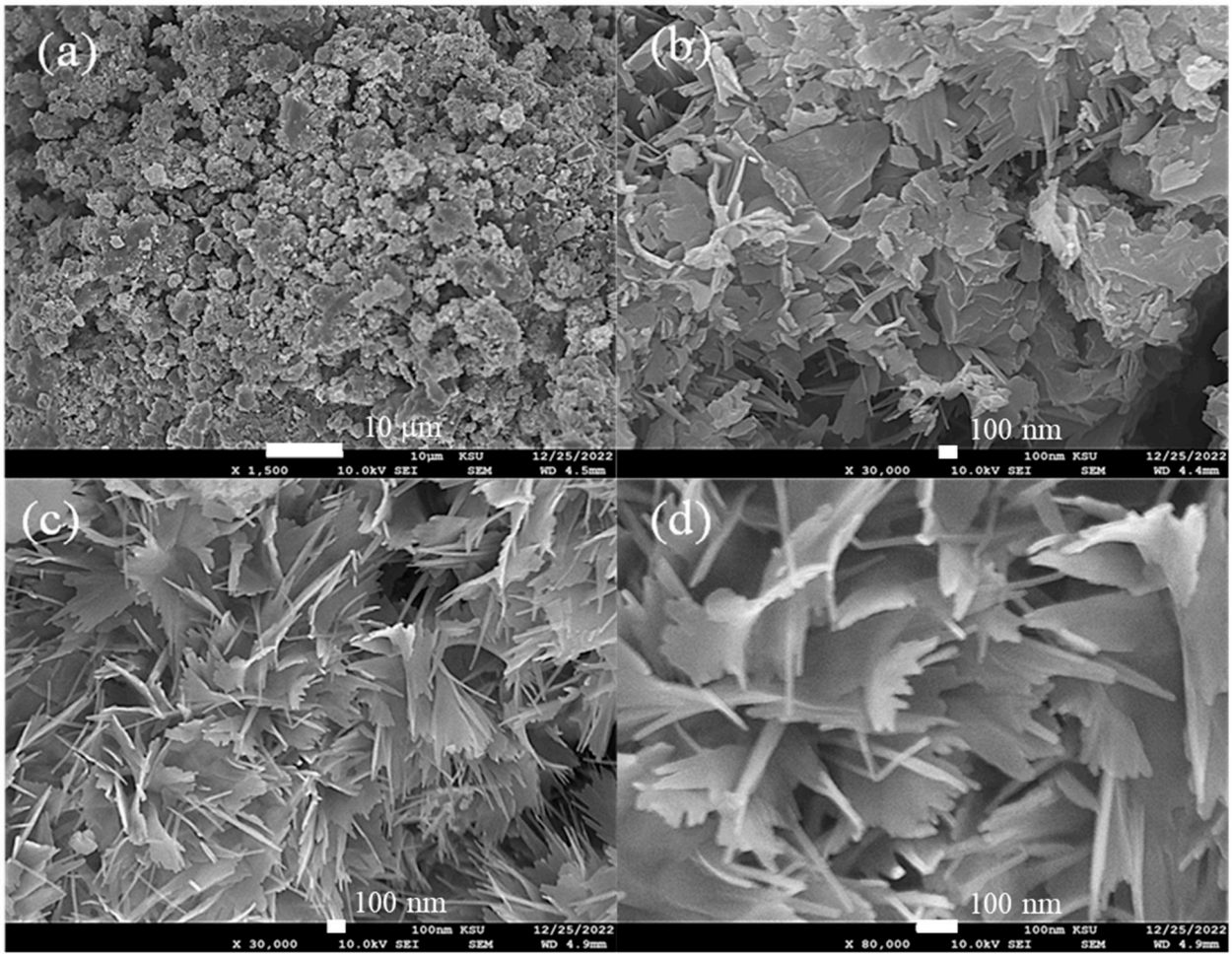

Figure 2. The SEM images recorded for as-prepared $CsNiVF_6$, at different magnifications, (**a**) 1500×, (**b**) 30,000×, (**c**) 30,000× and (**d**) 80,000×.

The energy-dispersive X-ray spectroscopy (EDX) elemental analysis and mapping are presented in Figure 3 and Table 1. The EDX elemental analysis revealed the existence of Cs, Ni, V, and F elements at weight/atomic values of 36.26/10.65, 16.46/10.93, 14.5/11.08 and 32.78/67.34%, respectively (Table 1), approximately aligning with the molecular formula of $Cs_{1.09}Ni_{1.12}V_{1.12}F_{6.9}$ and the mapping in Figure 3.

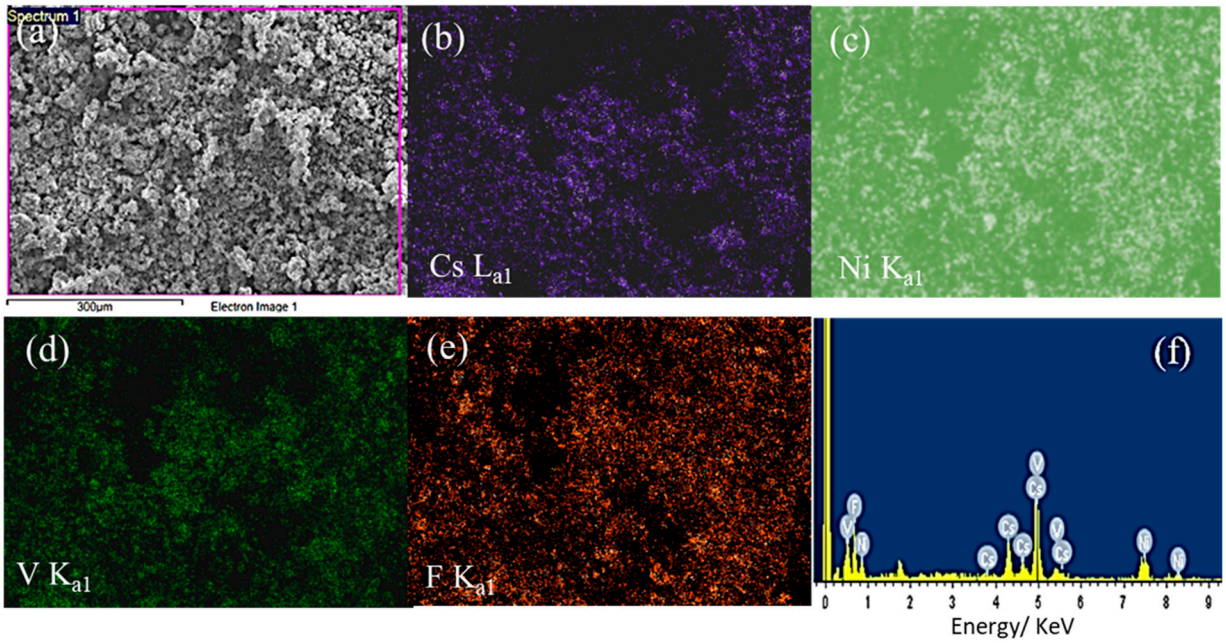

Figure 3. The EDX elemental analysis and mapping of the $CsNiVF_6$ catalyst; (**a**) SEM electron image; and corresponding X-ray elemental mapping of (**b**) F K_{a1}, (**c**) V K_{a1}, (**d**) Ni K_{a1}, (**e**) Cs L_{a1} and (**f**) EDX spectrum.

Table 1. The EDX elemental composition analysis of the as-prepared and spent $CsNiVF_6$ catalyst before and after use in urea electrolysis, respectively.

Element	wt. %	Atomic%	Mole Ratio	wt. %	Atomic%	Mole Ratio
Condition		**As-Prepared**			**After Use in Electrolysis**	
Cs	36.26	10.65	1.0	1.48	0.30	0.01
Ni	16.46	10.93	1.0	34.72	15.84	0.60
V	14.5	11.08	1.0	14.51	7.63	0.28
F	32.78	67.34	6.0	23.79	33.54	1.25
O	--	--	--	25.50	42.69	1.60

The X-ray photoelectron spectroscopy (XPS) surface analysis confirms the presence of cesium (Cs), nickel (Ni), vanadium (V), and fluorine (F) on the surface and provides an insight into the oxidation states of these elements. Figure 4 displays the XPS surface analysis of the $CsNiVF_6$ catalyst. The wide spectrum in Figure 4a reveals the characteristic peaks of the V 2p, Cs 3d, F 1s and Ni 2P spin orbits of the $CsNiVF_6$ catalyst. Additionally, surface contaminants of C 1s and O 1s were also observed at ~284.5 and 529.7 eV, respectively. The Cs 3d core spectrum in Figure 4b exhibits the well-resolved spin–orbit components (ΔE = 14.0 eV) of Cs 3d5/2 and Cs 3d3/2 at binding energies of 724.7 and 738.7 eV, respectively, indicating the presence of Cs(III) and Cs(IV) oxidation states. The Ni 2p core spectrum in Figure 4c reveals the well-resolved peaks corresponding to the Ni $2p_{3/2}$ and Ni $2p_{1/3}$ spin–orbits and satellite peaks at 856.8, 862.40 and 865.6 eV, respectively. The peak fitting analysis suggests the presence of Ni(II) and Ni(III) oxidation states in the structure of the $CsNiVF_6$ pyrochlore catalyst [49,51]. Similarly, the V 2p core spectrum in Figure 4d displays asymmetric and well-separated V $2p_{3/2}$ and V $2p_{1/2}$ states at binding

energies of 517.35 and 524.45 eV, respectively, with an energy separation value (ΔE) of 7.1 eV. The core fitted spectrum of F 1s in Figure 4e shows a main peak at 685.05 eV and a smaller one around 689.10 eV, suggesting the different chemical environments of the fluoride ions bonding to Ni or V, respectively, in the octahedral coordinate pyrochlore structure [40]. Finally, the core deconvoluted spectrum of O 1s shown in Figure 4f indicates that the first peak at a lower binding energy of 530.60 eV can be assigned to the surface O^{1-} species and that the second peak at 533.60 eV is related to the oxygen chemically adsorbed species (O^{chem}) on the surface [49,51].

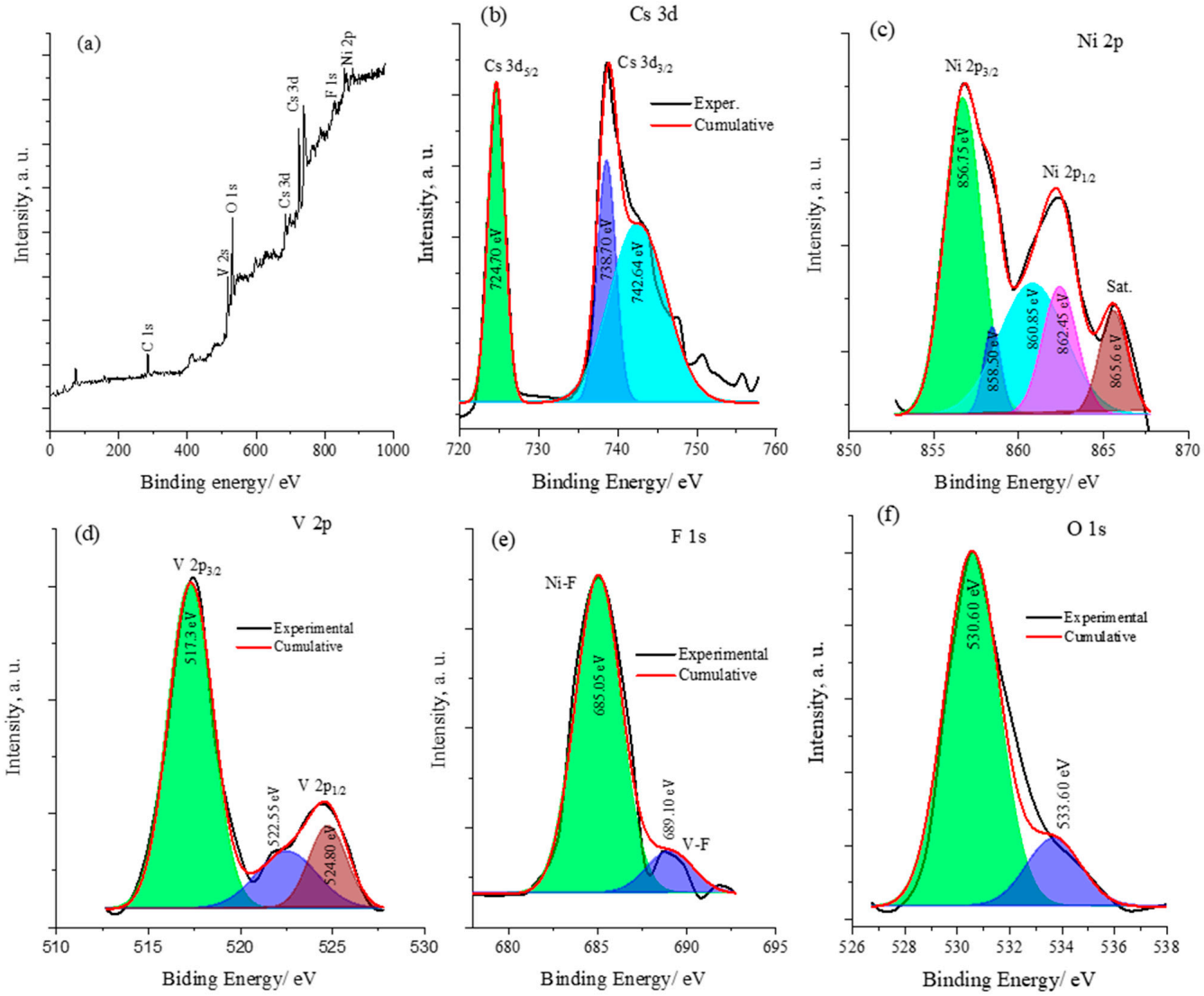

Figure 4. The XPS spectra analysis of the $CsNiVF_6$ catalyst (**a**) wide spectrum and the core spectra of (**b**) Cs 3d, (**c**) Ni 2p, (**d**) V 2p, (**e**) the F s1 peak, and (**f**) O 1s.

2.2. Electrochemical Behaviour and Activity of the $CsNiVF_6$ Pyrochlore Electrocatalyst for Urea Oxidation

To optimize the electrochemical performance of the catalyst, Figure 5 illustrates the electrochemical cyclic voltammetry at a scan rate of 50 mV/s for varying loadings (10, 20, 50 and 100 μg) of the $CNiVF_6$ catalyst in 1.0 M KOH solution. The CV results reveal the characteristic oxidation/reduction peaks of the Ni(II)/Ni(III) redox center at ~1.45/1.30 V vs. RHE. Notably, a gradual enhancement in current is observed with increasing catalyst loading, indicating an augmentation of the electroactive surface area and the reaction of the Ni(II)/Ni(III) active sites with hydroxide ions [53].

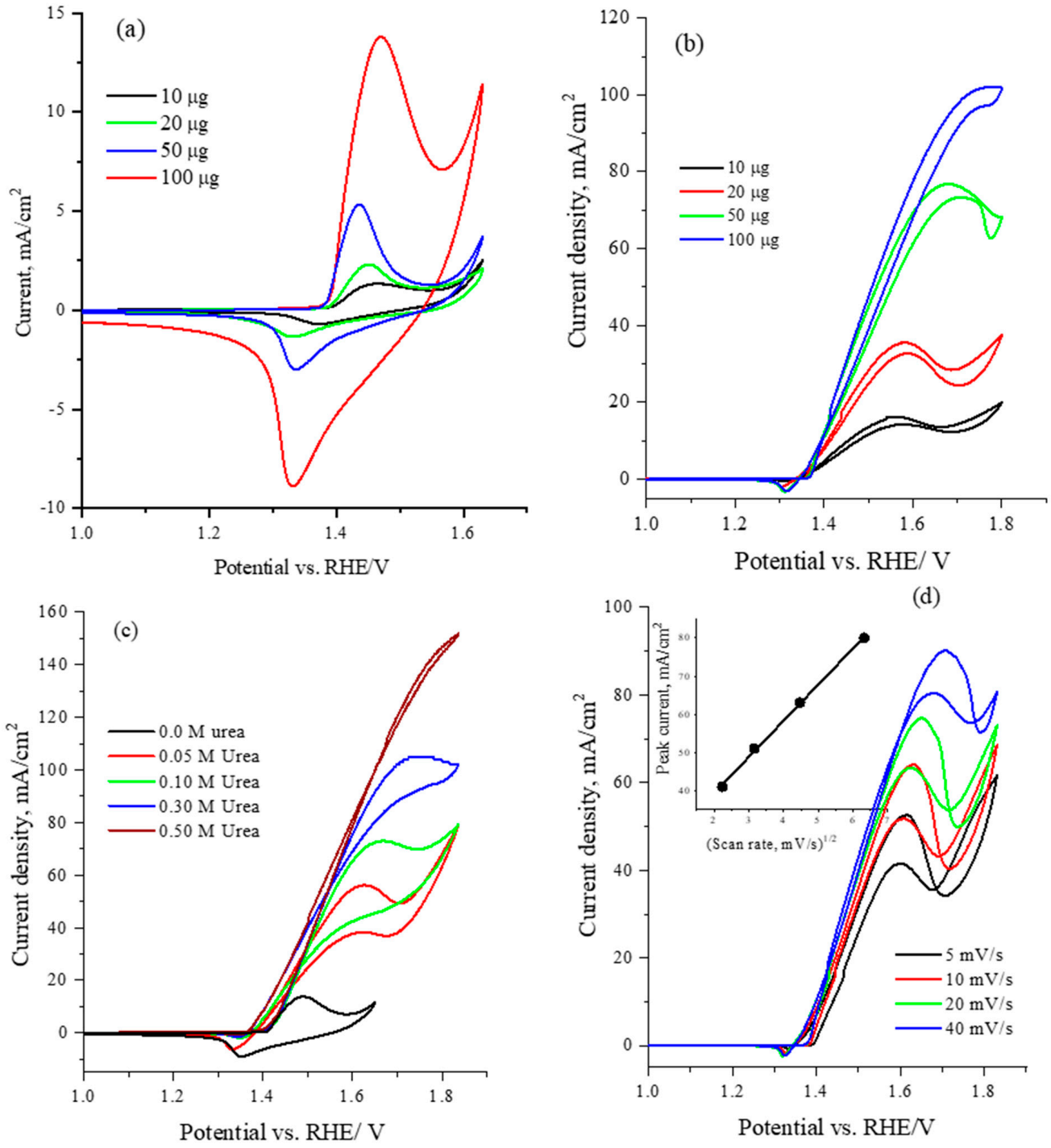

Figure 5. Cyclic voltammetry at 50 mV/s for CsNiVF6 catalyst loadings of 10, 20, 50 and 100 µg in (**a**) 1.0 M KOH solution, (**b**) 0.33 M urea in 1.0 M KOH solution, (**c**) CV for various urea concentrations in 1.0 M KOH solution using 100 µg of CsNiVF6 catalyst, and (**d**) the cyclic voltammetry obtained at different scan rates for 100 µg of CsNiVF6 catalyst in 0.33 M urea in 1.0 M KOH solution. The inset shows the correlation between the urea oxidation peak current density and the square root of the scan rate.

The optimization of the electrochemical performance of the $CsNiVF_6$ catalyst for urea oxidation was investigated by varying both the catalyst loading and urea concentration. Figure 5b displays the cyclic voltammetry (CV) profiles at a scan rate of 50 mV/s for different loadings of the $CsNiVF_6$ catalyst in a solution containing 0.33 M urea and

1.0 M KOH. Upon examining various catalyst loadings (10, 20, 50, 100 µg), a discernible trend emerges, wherein the electrochemical urea oxidation current exhibits a significant increase at an onset potential of 1.35 V vs. RHE, with further enhancement observed when scanning to more positive potentials is performed and the catalyst loading is increased. The observed increase in the anodic peak current with increasing catalyst loading emphasizes the high activity of the $CsNiVF_6$ anode in the electrochemical oxidation of the alkaline urea solution. This enhanced activity can be attributed to the presence of Ni(II)/Ni(III) active sites, which catalyze the urea reaction following the well-documented electrochemical-chemical (EC) mechanism, as illustrated by the following reactions: [11,13–16,21,55].

$$2Ni(II) + 6OH^- \rightarrow 2Ni(III)\ (OH)_3 + 6e^- \quad (1)$$

$$CO(NH_2)_{2\ (aq)} + 2Ni\ (III)\ (OH)_3 \rightarrow 2Ni(II) + N_{2\ (g)} + CO_{2\ (g)} + 5H_2O_{\ (l)} \quad (2)$$

$$\text{Net reaction: } CO(NH_2)_{2\ (aq)} + 6OH^- \rightarrow 5H_2O\ (l) + N_{2\ (g)} + CO_{2\ (g)} + 6e^- \quad (3)$$

Moreover, the disappearance of the reduction peak of Ni(III)/Ni(II) around 1.3 V vs. RHE in the reverse scan confirms the EC mechanism and consumption of Ni(III) active sites during urea oxidation, as indicated by Equation (2). Figure 5c presents the cyclic voltammograms for optimizing the urea concentration using 100 µg of $CsNiVF_6$ pyrochlore catalyst at a scan rate of 50 mV/s in 1.0 M KOH solution. The electrochemical urea oxidation current demonstrates a gradual augmentation with increasing urea concentration. In particular, the urea concentration of 0.50 M emerges as optimal, yielding a noteworthy current mass activity of ~1500 mA mg^{-1}, recorded at 1.8 V vs. RHE. The study employs cyclic voltammetry (CV) to provide critical insights on the effect of various scan rates (5, 10, 20, 50 mV/s), as shown in Figure 5d. The results emphasize the increase in the urea oxidation current with higher scan rates. Specifically, the correlation of the peak current around 1.6 V vs. RHE was found to be linearly increased with the square root of the scan rate, confirming that the urea oxidation reaction mainly proceeds under diffusion control, as shown in the inset of Figure 5d. Moreover, the observed shifts in the urea oxidation peak and the increase in current underscore the scan rate's role in modulating the electrochemical behavior.

Electrochemical impedance spectroscopy (EIS) analysis was conducted for the $CsNiVF_6$ catalyst/electrolyte interface during urea oxidation in the 1.0 M KOH solution to evaluate the charge transfer resistance during the electrochemical reaction. Figure 6a presents the Nyquist plots obtained for 100 µg of the $CsNiVF_6$ nanosheet catalyst in a 0.33 urea and 1.0 M KOH solution at applied potentials of 1.45, 1.55 and 1.65 V vs. Ag/AgCl, across a frequency range of 0.1 to 100 kHz. In the inset of Figure 6a, the impedance spectra for the $CsNiVF_6$ catalyst are fitted to an equivalent circuit model using Zsim 3.20 software, featuring a series combination of solution ohmic resistance (R_s), charge transfer resistance (R_{ct}), and double-layer capacitance (C_{dl}). Additionally, the inset in Figure 6a shows the zoom-in Nyquist plots at the high-frequency region at an applied potential of 1.45, 1.55 and 1.65 V. Table 2 reports the impedance parameter values obtained by fitting the Nyquist to the equivalent circuit shown in the inset of Figure 6a. Moreover, the values of the impedance parameters of charge transfer resistance (R_1), double-layer capacitance (Q_1), and solution resistance (R_s) obtained from the equivalent circuit fitting are reported in Table 2. Observations from the Nyquist plots and Table 2 reveal that for the $CsNiVF_6$, the radii of the arcs, indicative of the charge transfer resistance (R_{ct}), decreased at a more positive applied potential and that values of 5.50, 3.74 and 3.25 ohm were achieved at 1.45, 1.55 and 1.65 V vs. RHE, respectively. This suggests that the $CsNiVF_6$ catalyst exhibits enhanced charge transfer, reaction kinetics and electrochemical performance for urea oxidation at a more positive potential.

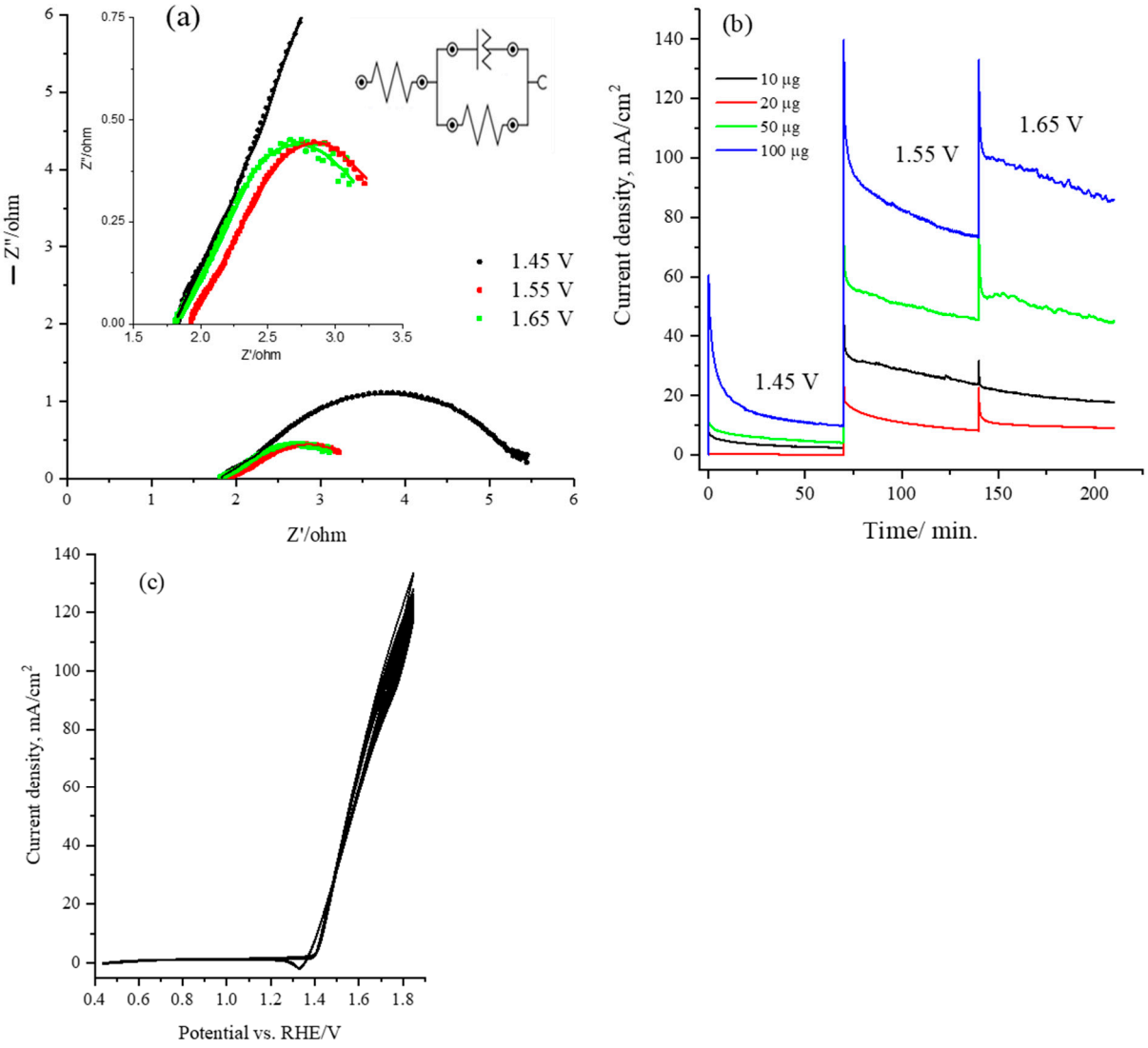

Figure 6. (**a**) Nyquist plot obtained for 100 µg of the $CsNiVF_6$ catalyst recorded at 1.45, 1.55, and 1.65 vs. HRE and within the frequency range of 0.1 to 100 kHz at an amplitude of 10 mV; (**b**) chronoamperometry for $CsNiVF_6$ catalyst recorded at various potentials (1.45, 1.55, and 1.65 vs. HRE) in 1.0 M KOH containing 0.33 M urea solution and using various loadings (10, 20, 50, 100 µg); and (**c**) long-term stability test performed by cyclic voltammetry at 50 mV/s for 100 cycles of 100 µg of $CsNiVF_6$ catalyst in 0.33 M urea and 1.0 M KOH solution.

Table 2. EIS parameters of the $CsNiVF_6$ catalyst obtained through the fitted equivalent circuit at different potentials.

Potential/V vs. RHE	Rs/ohm	C_{dl}/mF	R_{ct}, ohm
1.45	1.75	17.4	5.50
1.55	1.80	21.6	3.74
1.65	1.85	28.3	3.25

The stability and performance of the $CsNiVF_6$ catalyst in electrolysis were assessed through chronoamperometry and cyclic voltammetry for urea oxidation in a 1.0 M KOH solution. Figure 6b illustrates the chronoamperometry for the oxidation of 0.33 M urea using various loadings of the $CsNiVF_6$ catalyst (10, 20, 50 and 100 µg) at different applied potentials in a 1.0 M KOH solution containing 0.33 M urea. Notably, there was a substantial increase in the urea oxidation current density at a higher applied potential and $CsNiVF_6$

catalyst loading. In particular, the mass activity of the $CsNiVF_6$ catalyst with a 100 µg loading reached an impressive ~0.90 A mg^{-1} at 1.65 V vs. RHE after 3.0 h of electrolysis. Moreover, the urea oxidation current in the $CsNiVF_6$ catalyst retained about 88% of its original values at the end of the 3 h electrolysis, which could be attributed to the catalyst being physically detached from the carbon paper substrate and/or morphological and composition changes (see below). Moreover, Figure 6c shows the long-term stability test performed by cyclic voltammetry at 50 mV/s for 100 cycles of 100 µg of $CsNiVF_6$ catalyst in 0.33 M urea and 1.0 M KOH solution. The multicycle voltammogram confirmed that the urea oxidation current in the $CsNiVF_6$ catalyst slightly decreased after the 100 cycles within the potential range (1.40–1.80 V), signifying excellent cycling stability.

For comparison, Table 3 reports the mass/specific activity values and conditions of the $CsNiVF_6$ catalyst for the urea oxidation reaction compared to the state-of-the-art nickel-based catalyst reported in the literature [56–58]. The $CsNiVF_6$ nanosheets exhibit a urea oxidation mass activity of ~1500 mA mg^{-1} at a potential of 1.80 V vs. RHE, which is superior and/or comparable to the state-of-the-art catalysts reported in the literature, such as $KNiAlF_6$ nanosheets (~395 mA mg^{-1}) [53], Ni foam-supported OM-NiO nanosheets (450 mA mg^{-1}) [58] and nickel hydroxide nanoflakes (~1295 mA mg^{-1}) [32].

Table 3. Comparison between the urea oxidation activity performance of the $CsNiVF_6$ catalyst and the state-of-the-art nickel-based catalysts reported in the literature, calculated from the cyclic voltammetry at specified potentials and conditions.

Anodic Materials	Mass Activity, mA mg^{-1} (Specific Activity, mA/cm^2) vs. RHE	Reference
Ni^{3+}-rich $Ni(OH)_2$/C–NH_2/GCE	(91.72) [a] at 1.65 V [c]	[56]
Nickel hydroxide nanoflakes	~1295 [a] at 1.55 V [c], 1.0 M NaOH	[32]
$KNiAlF_6$ nanosheets	~395 [a] at 1.65 V [c]	[53]
β-$Ni(OH)_2$-CNTs (80 °C)/hydrothermal reaction	(98.5) [a] at 1.65 V [c]	[57]
S-doped β-$Ni(OH)_2$ nanosheet	(~37) [a] at 1.60 V [c]	[28]
Ni foam-supported OM-NiO nanosheets	450 [b] at 1.65 V [c]	[58]
$CsNiVF_6$ nanosheet	~1500 [a] at 1.8 V [c]	This work

[a] Scan rate = 50 mV/s, [b] Scan rate = 10 mV/s, [c] the potential measured vs. Ag/AgCl reference electrode.

Moving on, the $CsNiVF_6$ spent catalyst underwent morphological and compositional analysis after being used in the stability test of urea electrolysis. Figure 7 shows the SEM and EDX elemental analysis of the $CsNiVF_6$ catalyst after being subjected to the urea electrolysis process at 0.60 V vs. Ag/AgCl in a 0.33 M urea/1.0 M KOH solution for 3 h, as depicted above. The SEM image in Figure 7a provides compelling evidence of substantial changes in the nanosheet morphology, with the noticeable self-reconstruction of swelling and the coalescence of the nanosheet structures, ultimately forming irregularly overlapped microparticles. Upon closer examination of the microparticles, the high-magnification SEM image in Figure 7b reveals a morphology resembling uniform nanoparticles with an average diameter of 30 nm. Additionally, the EDX elemental analysis shown in Figure 7c reveals significant structural and chemical composition transformation in the $CsNiVF_6$ catalyst after being used in the urea electrolysis process, containing Cs, Ni, V, F, and O elements at wt.% of 1.48, 34.72, 14.51, 23.79 and 25.50%, respectively. Notably, the elemental composition of the $CsNiVF_6$ catalyst has changed, particularly with the oxygen content reaching 25.50 wt.% due to the electrochemical oxidation in the alkaline urea solution. Moreover, the cesium and fluorine wt.% decreased notably from 22.82 to 1.48% and from 32.78 to 23.79, respectively, suggesting the leaching of the pyrochlore structure after the catalyst had been used in the electrolysis process. This suggests that the phase transformation of the spent $CsNiVF_6$ catalyst into oxyfluoride has a chemical composition of $Cs_{0.01}Ni_{0.60}V_{0.28}O_{1.6}F_{1.25}$ after the urea oxidation stability test. Such a change in the structure and composition of the spent $CsNiVF_6$ catalyst could be related to the NiV–OF bonding and the formation of new $NiF_x(OH)_y$ and $VF_x(OH)_y$ catalytic active sites [49,58].

Therefore, despite the significant alterations in the catalyst's morphology and composition, it exhibited a reasonable urea oxidation current and activity retention of 88% compared to the original values, as depicted in Figure 6b, after its exposure to urea electrolysis for more than 3.0 h.

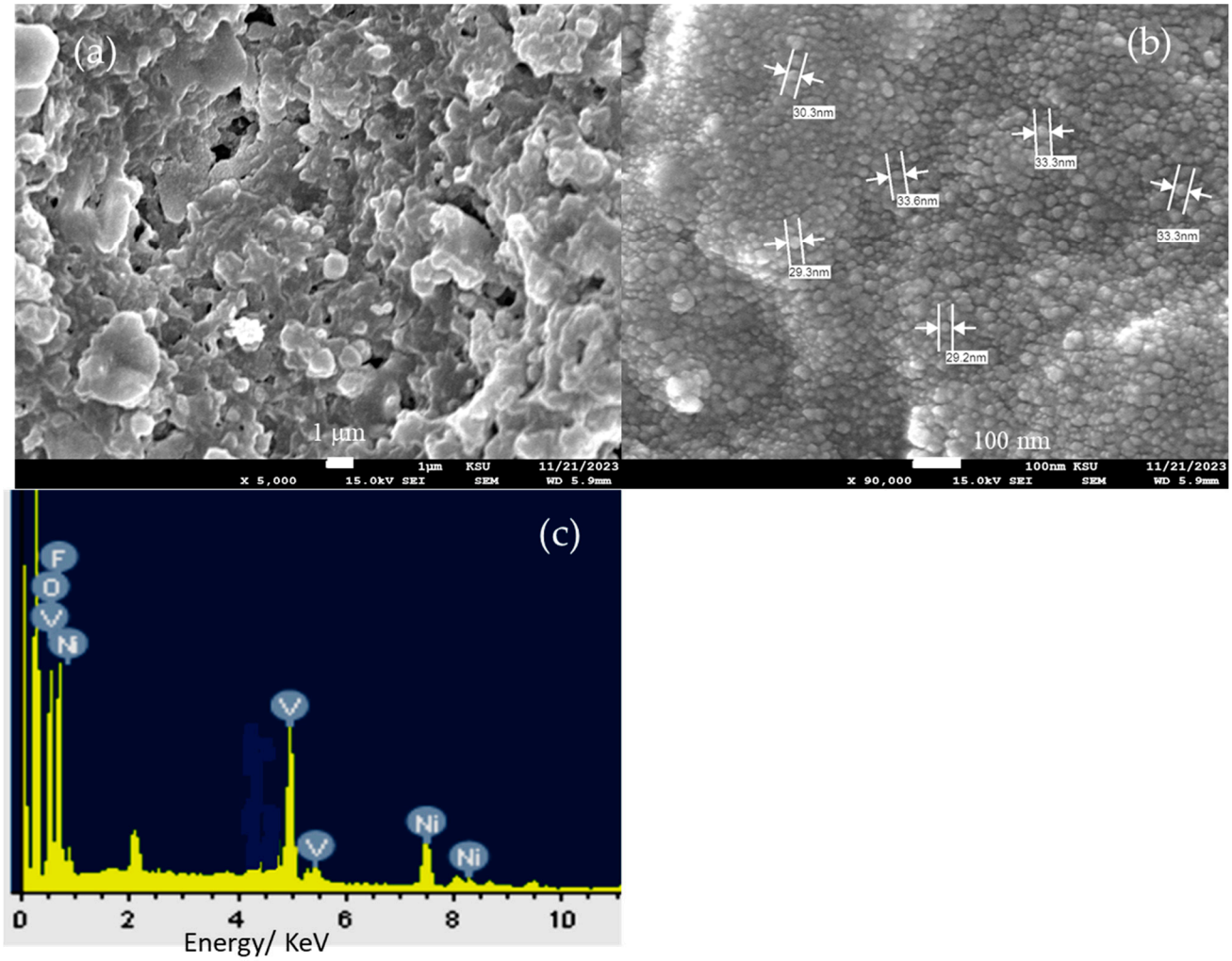

Figure 7. SEM images at different magnifications, (**a**) 5000×, (**b**) 90,000× and (**c**) EDX elemental analysis of the $CsNiVF_6$ catalyst after being used in the urea electrolysis process.

2.3. Hydrogen Production Rate Using $CsNiVF_6$ Anode during Urea Electrolysis

Finally, the rate of hydrogen production at the cathode (bare-nickel foam) using the $CsNiVF_6$ anode loaded on carbon paper (0.450 mg/cm^2) was monitored during urea electrolysis (0.33 M) in 1.0 M KOH solution using the homemade H-shape electrolyzer, as shown in Figure 8. The data in Figure 8 show the cathodic hydrogen production rate (HPR) during urea electrolysis using a $CsNiVF_6$ catalyst at the applied voltages of 1.8 and 2.0 in 1.0 M KOH solution, both in the presence and absence of 0.33 M urea. The results reveal that in pure 1.0 M KOH solution, the HPR reaches 6.30 and 23.20 µmol/min, while in the presence of 0.33 M urea, it increases to 12.25 and 39.15 µmol/min at applied potentials of 1.8 and 2.0 V, respectively. Remarkably, the rate of hydrogen production nearly doubles upon the addition of urea to the alkaline solution, indicating its potential as an electrolyte in a cost-effective hydrogen production process. Furthermore, the hydrogen production rate triples with the increase in the applied voltage from 1.8 to 2.0 V, suggesting the potential of the $CsNiVF_6$ catalyst for efficient and economical green hydrogen production.

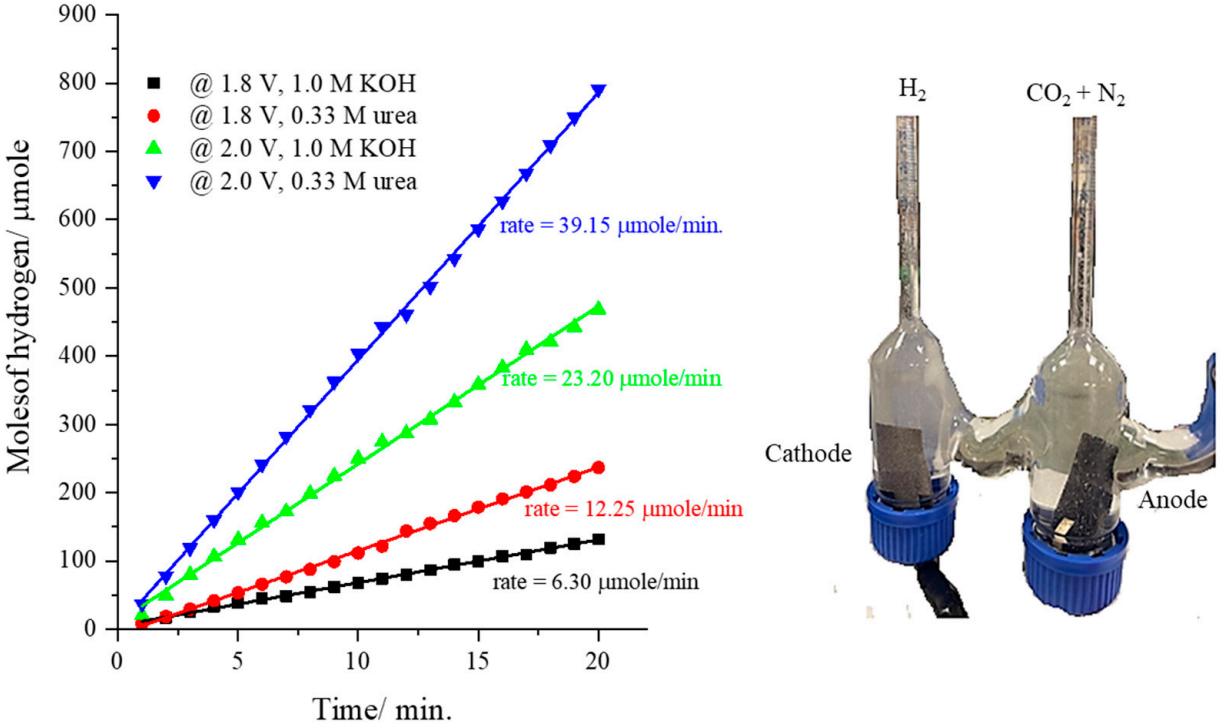

Figure 8. The cathodic hydrogen production rate at an applied potential of 1.8 and 2.0 V using the $CsNiVF_6$ catalyst as an anode in pure 1.0 M KOH and the presence of 0.33 M urea.

3. Materials and Methods

3.1. Chemicals and Materials

Analytical-grade cesium hydrogen fluoride (CsF_2H), nickel fluoride (NiF_2), and vanadium fluoride were obtained from Sigma-Aldrich (Saint Louis, MO, USA). Urea ($CO(NH_2)_2$) was sourced from AVONCHEM Corp (Cheshire, UK), while potassium hydroxide pellets (KOH, purity >99%, Loba Chemie PVT Ltd., Mumbai, India) and isopropanol were purchased from the AnalaR group (Princeton, NJ, USA). Nafion solution (10% w/v) was obtained from Merck (Boston, MA, USA), and 37% hydrochloric acid (Sigma) was also utilized. All chemicals were used as received without further purification. Deionized water (DI, 18 MU resistivity) obtained using a Milli-Q ultrapure water purification system (18.2 MΩ resistivity) was used throughout this work.

3.2. Synthesis of $CsNiVF_6$ Catalyst

The nanostructured cesium–nickel–vanadium fluoride $CsNiVF_6$ catalyst was synthesized from fluoride-based precursors using thermal solid-phase synthesis, following procedures reported elsewhere [50]. Briefly, CsF_2H, NiF_2, and VF_3 were mixed and ground together at a molar ratio of 1:1:1, respectively. The mixture was then heated to 900 °C under a nitrogen atmosphere in a platinum crucible for 24 h. Subsequently, the product was cooled to room temperature, and subjected to further heating at 900 °C for an additional 72 h. After cooling in an open atmosphere, the product was washed several times with deionized water to remove residual raw materials, followed by overnight drying in an oven at 60 °C.

3.3. Physiochemical Characterizations of $CsNiVF_6$ Catalyst

The crystal structure of the $CsNiVF_6$ catalyst was determined using X-ray diffraction (XRD) analysis, performed on a Rigaku Miniflex 600 instrument (Rigaku Corporation, Tokyo, Japan) with a $CuK_{\alpha 1}$ irradiation source operated at 40 kV and 15 mA. The surface morphology was examined using scanning electron microscopy (SEM) on an FEI Quanta 250 instrument operated at 15–20 kV. The X-ray photoelectron spectroscopy (XPS) charac-

terization spectra were recorded using an Escalab 250 XPS spectrometer (Thermo Fisher, Waltham, MA, USA).

3.4. Electrochemical Characterization Measurements

All electrochemical measurements were conducted using an Auto-lab potentiostat/galvanostat (μ3Auto71211) instrument. A three-electrode electrochemical cell was employed, comprising a carbon paper (CP, ®SIGRACET, grade GDL-24BC, Fuel Cell Store, TX, USA) working electrode (1 × 1 cm^2), a graphite counter electrode (1 × 1 cm^2), and Ag/AgCl as the reference electrode. The working electrode potential was normalized to the hydrogen reference electrode (HRE) using the equation ($E_{HRE}/V = E_{Ag/AgCl} + 0.198 + 0.059$ pH). Electrochemical measurements of the catalyst were conducted in an alkaline solution at predefined concentrations and in the absence and presence of various concentrations of urea using cyclic voltammetry (CV), chronoamperometry (CA), and electrochemical impedance analysis techniques. The catalyst ink was prepared by mixing 10 mg of the $CsNiVF_6$ or reference catalyst with 1.0 mL of isopropanol/distilled water (1:1, *v*/*v*) and adding 10 μL of Nafion solution (1.0 wt.%) in a glass vial. The resulting mixture was sonicated for 15 min at room temperature. Various loadings of the obtained suspension were physically cast onto the carbon paper or nickel foam substrate, followed by drying with a hot air gun.

3.5. The Volumetric Determination of the Hydrogen Gas Production Rate

The volumetric determination of the hydrogen gas production rate was performed using a homemade H-shaped glass electrolyzer (Gulf Scientific Glass Industry WLL, Al Hidd, Bahrain), consisting of anodic and cathodic compartments connected by a central channel, as shown in the inset of Figure 8. The anode comprised catalyst/CP (2.0 × 3.0 cm^2) (about 0.50 mg/cm^2) coated on both sides, while the cathode consisted of bare nickel foam (2.0 × 3.0 cm^2). Surface cleaning of the nickel foam (3 × 3 cm^2) was performed using a 0.1 M hydrochloric acid (HCl) solution in an ultrasound bath for 5 min. Subsequently, the nickel foam was rinsed with deionized water and absolute ethanol, each for 5 min. The electrolyzer was filled with 2.0 M KOH or 0.33 M urea solution up to the zero-mark level of the cathodic compartment. Urea electrooxidation at the anode was initiated using a $CsNiVF_6$ catalyst by applying a suitable bias voltage (1.8, and 2.0 V) controlled by the power supply, leading to the evolution of hydrogen gas bubbles at the nickel foam cathode. The volume of hydrogen gas was monitored at a regular interval until the desired reaction time was achieved.

4. Conclusions

In summary, this study successfully synthesized a nanosheet of a $CsNiVF_6$ pyrochlore catalyst using solid-phase synthesis and explored its efficacy as an electrocatalyst for urea oxidation and hydrogen production in alkaline media. Utilizing XRD and SEM analysis, the nanosheet structure of $CsNiVF_6$ was characterized, revealing a pyrochlore cubic defected nanosheet structure with an average thickness ranging from 57.6 to 93.8 nm. The electrochemical analysis of the $CsNiVF_6$ electrode, particularly the cyclic voltammetry and chronoamperometry curves, showed a urea oxidation current density of up to 150 mA/cm^2 at a potential of 1.8 V vs. RHE, demonstrating its promising catalytic activity as well as durability in the urea oxidation reaction. Moreover, the $CsNiVF_6$ catalyst exhibited a notable enhancement in hydrogen production via electrolysis across various electrolyte solutions. The study revealed a direct correlation between the hydrogen production volume and applied voltage, with the highest volume (39.15 μmol/min) observed in the 1.0 M KOH and 0.33 M urea solution at 2.0 V. Notably, the addition of urea to the electrolyte solution augmented hydrogen production, particularly at lower voltages. However, the spent $CsNiVF_6$ electrode exhibits a significant composition, morphology and phase transformation into oxyfluoride, with a chemical composition of $Cs_{0.01}Ni_{0.60}V_{0.28}O_{1.6}F_{1.25}$, after being used in the urea electrolysis process. Despite this, the catalysts maintained a stable urea oxidation current with an activity retention of 88% compared to the original

value. The catalyst composition alteration and fluoride etching during the urea electrolysis process induced more active and defective sites of mixed Ni/V redox centres that benefited and enhanced the kinetics of the urea oxidation reaction. The further refinement of the electrolyte solution and the optimization of operating conditions could play a pivotal role in enhancing the efficiency and cost reduction of sustainable green hydrogen production systems.

Author Contributions: M.A.G.: Conceptualization, Formal analysis, Writing—review and editing, Supervision, Funding acquisition; A.M.A.-M.: Methodology, Investigation; K.A.A.: Data curation, Validation, Writing; M.O.A.: Investigation, Methodology, Visualization, Validation. All authors have read and agreed to the published version of the manuscript.

Funding: This work funded by Innovation initiative from the Ministry of Education and King Saud University for Institutional Funding for the Research and Innovation Program, Project no IFKSUDR_E125.

Data Availability Statement: Data are contained within the article.

Acknowledgments: The authors would like to express their sincere gratitude to the Research and Innovation initiative from the Ministry of Education and King Saud University for Institutional Funding for the Research and Innovation Program, Project no IFKSUDR_E125.

Conflicts of Interest: The authors declare no conflicts of interest.

References

1. Song, J.; Wei, C.; Huang, Z.-F.; Liu, C.; Zeng, L.; Wang, X.; Xu, Z.J. A review on fundamentals for designing oxygen evolution electrocatalysts. *Chem. Soc. Rev.* **2020**, *49*, 2196–2214. [CrossRef]
2. Xia, W.; Mahmood, A.; Liang, Z.; Zou, R.; Guo, S. Earth-Abundant Nanomaterials for Oxygen Reduction. *Angew. Chem. Int. Ed.* **2016**, *55*, 2650–2676. [CrossRef]
3. Wang, Z.L.; Xu, D.; Xu, J.J.; Zhang, X.B. Oxygen Electrocatalysts in Metal-Air Batteries: From Aqueous to Nonaqueous Electrolytes. *Chem. Soc. Rev.* **2014**, *43*, 7746–7786. [CrossRef]
4. Song, H.; Luo, S.; Huang, H.; Deng, B.; Ye, J. Solar-Driven Hydrogen Production: Recent Advances, Challenges, and Future Perspectives. *ACS Energy Lett.* **2022**, *7*, 1043–1065. [CrossRef]
5. Zhang, Y.-L.; Goh, K.; Zhao, L.; Sui, X.-L.; Gong, X.-F.; Cai, J.-J.; Zhou, Q.-Y.; Zhang, H.-D.; Li, L.; Kong, F.-R.; et al. Advanced non-noble materials in bifunctional catalysts for ORR and OER toward aqueous metal–air batteries. *Nanoscale* **2020**, *12*, 21534–21559. [CrossRef]
6. Burke, M.S.; Enman, L.J.; Batchellor, A.S.; Zou, S.; Boettcher, S.W. Oxygen Evolution Reaction Electrocatalysis on Transition Metal Oxides and (Oxy)Hydroxides: Activity Trends and Design Principles. *Chem. Mater.* **2015**, *27*, 7549–7558. [CrossRef]
7. Guan, D.; Wang, B.; Zhang, J.; Shi, R.; Jiao, K.; Li, L.; Wang, Y.; Xie, B.; Zhang, Q.; Yu, J.; et al. Hydrogen society: From present to future. *Energy Environ. Sci.* **2023**, *16*, 4926–4943. [CrossRef]
8. Lewis, N.S.; Nocera, D.G. Powering the planet: Chemical challenges in solar energy utilization. *Proc. Natl. Acad. Sci. USA* **2006**, *103*, 15729–15735. [CrossRef]
9. Tahir, M.; Pan, L.; Idrees, F.; Zhang, X.; Wang, L.; Zou, J.J.; Wang, Z.L. Electrocatalytic Oxygen Evolution Reaction for Energy Conversion and Storage: A Comprehensive Review. *Nano Energy* **2017**, *37*, 136–157. [CrossRef]
10. Jamesh, M.I. Recent progress on earth abundant hydrogen evolution reaction and oxygen evolution reaction bifunctional electrocatalyst for overall water splitting in alkaline media. *J. Power Sources* **2016**, *333*, 213–236. [CrossRef]
11. Boggs, B.K.; King, R.L.; Botte, G.G. Urea electrolysis: Direct hydrogen production from urine. *Chem. Commun.* **2009**, *32*, 4859. [CrossRef]
12. Wang, G.M.; Ling, Y.C.; Lu, X.H.; Wang, H.Y.; Qian, F.; Tong, Y.X.; Li, Y. A review on nanomaterials for environmental remediation. *Energy Environ. Sci.* **2012**, *5*, 8215. [CrossRef]
13. Lan, R.; Tao, S.W.; Irvine, J.T.S. A direct urea fuel cell–power from fertilizer and waste. *Energy Environ. Sci.* **2010**, *3*, 438. [CrossRef]
14. Ding, R.; Qi, L.; Jia, M.J.; Wang, H.Y. Facile synthesis of mesoporous spinel $NiCo_2O_4$ nanostructures as highly efficient electrocatalysts for urea electro-oxidation. *Nanoscale* **2014**, *6*, 1369. [CrossRef]
15. Kakati, N.; Maiti, J.; Lee, K.S.; Viswanathan, B.; Yoon, Y.S. Electrochemical oxidation of urea on electrodeposited nickel nanoparticles for potential use in a direct urea fuel cell. *Electrochim. Acta* **2017**, *240*, 175. [CrossRef]
16. Zhu, D.D.; Guo, C.X.; Liu, J.L.; Wang, L.; Du, Y.; Qiao, S.Z. Two-dimensional metal–organic frameworks with high oxidation states for efficient electrocatalytic urea oxidation. *Chem. Commun.* **2017**, *53*, 10906. [CrossRef]
17. Singh, R.K.; Schechter, A. Electrochemical investigation of urea oxidation reaction on β $Ni(OH)_2$ and $Ni/Ni(OH)_2$. *Electrochim. Acta* **2018**, *278*, 405–411. [CrossRef]

18. Yu, E.H.; Wang, X.; Krewer, U.; Li, L.; Scott, K. Direct oxidation alkaline fuel cells: From materials to systems. *Energy Environ. Sci.* **2012**, *5*, 5668–5680. [CrossRef]
19. Yan, W.; Wang, D.; Botte, G.G. Electrochemical decomposition of urea with Ni-based catalysts. *Appl. Catal. B* **2012**, *127*, 221–226. [CrossRef]
20. Kojima, S.; Bohner, A.; von Wiren, N. Molecular mechanisms of urea transport in plants. *J. Membr. Biol.* **2006**, *212*, 83–91. [CrossRef]
21. Vedharathinam, V.; Botte, G.G. Understanding the electro-catalytic oxidation mechanism of urea on nickel electrodes in alkaline medium. *Electrochim. Acta* **2012**, *81*, 292–300. [CrossRef]
22. Vedharathinam, V.; Botte, G.G. Direct evidence of the mechanism for the electro-oxidation of urea on $Ni(OH)_2$ catalyst in alkaline medium. *Electrochim. Acta* **2013**, *108*, 660–665. [CrossRef]
23. Lu, S.; Zheng, X.; Fang, L.; Yin, F.; Liu, H. Rational engineering design of nickel hydroxides for urea oxidation reaction: A mini review. *Electrochem. Commun.* **2023**, *157*, 107599. [CrossRef]
24. Yu, J.; Li, Z.; Wang, C.; Xu, X.; Liu, T.; Chen, D.; Shao, Z.; Ni, M. Engineering advanced noble-metal-free electrocatalysts for energy-saving hydrogen production from alkaline water via urea electrolysis. *J. Colloid Interface Sci.* **2024**, *661*, 629–661. [CrossRef] [PubMed]
25. Wang, D.; Yan, W.; Botte, G.G. Exfoliated nickel hydroxide nanosheets for urea electrolysis. *Electrochem. Commun.* **2011**, *13*, 1135. [CrossRef]
26. Ji, R.Y.; Chan, D.S.; Jow, J.J.; Wu, M.S. Formation of open-ended nickel hydroxide nanotubes on three-dimensional nickel framework for enhanced urea electrolysis. *Electrochem. Commun.* **2013**, *29*, 21. [CrossRef]
27. Liang, Y.H.; Liu, Q.; Asiri, A.M.; Sun, X.P. Enhanced electrooxidation of urea using $NiMoO_4 \cdot xH_2O$ nanosheet arrays on Ni foam as anode. *Electrochim. Acta* **2015**, *153*, 456. [CrossRef]
28. Zhu, X.J.; Dou, X.Y.; Dai, J.; An, X.D.; Guo, Y.Q.; Zhang, L.D.; Tao, S.; Zhao, J.Y.; Chu, W.S.; Zeng, X.C.; et al. Metallic Nickel Hydroxide Nanosheets Give Superior Electrocatalytic Oxidation of Urea for Fuel Cells. *Chem. Int. Ed.* **2016**, *55*, 12465. [CrossRef] [PubMed]
29. Saguì, N.A.; Ström, P.; Edvinsson, T.; Pehlivan, İ.B. Nickel Site Modification by High-Valence Doping: Effect of Tantalum Impurities on the Alkaline Water Electro-Oxidation by NiO Probed by Operando Raman Spectroscopy. *ACS Catal.* **2022**, *12*, 6506–6516. [CrossRef]
30. Yan, W.; Wang, D.; Diaz, L.A.; Botte, G.G. Nickel nanowires as effective catalysts for urea electro-oxidation. *Electrochim. Acta* **2014**, *134*, 266–271. [CrossRef]
31. Wang, D.; Yan, W.; Vijapur, S.H.; Botte, G.G. Enhanced electrocatalytic oxidation of urea based on nickel hydroxide nanoribbons. *J. Power Sources* **2012**, *217*, 498–502. [CrossRef]
32. Ghanem, M.A.; Al-Mayouf, A.M.; Singh, J.P.; Arunachalam, P. Concurrent deposition and exfoliation of nickel hydroxide nanoflakes using liquid crystal template and their activity for urea electrooxidation in alkaline medium. *Electrocatalysis* **2017**, *8*, 16–26. [CrossRef]
33. Shen, Z.; Qu, M.; Shi, J.; Oropeza, F.E.; de la Peña O'Shea, V.A.; Gorni, G.; Tian, C.M.; Hofmann, J.P.; Cheng, J.; Li, J.; et al. Correlating the electronic structure of perovskite $La_{1-x}SrxCoO_3$ with activity for the oxygen evolution reaction: The critical role of Co 3d hole state. *J. Energy Chem.* **2022**, *65*, 637–645. [CrossRef]
34. Ghanem, M.A.; Amer, M.S.; Arunachalam, P.; Al-Mayouf, A.M.; Weller, M.T. Role of rhodium doping into lanthanum cobalt oxide ($LaCoO_3$) perovskite and the induced bifunctional activity of oxygen evolution and reduction reactions in alkaline medium. *Arab. J. Chem.* **2022**, *15*, 104256. [CrossRef]
35. Suntivich, J.; May, K.J.; Gasteiger, H.A.; Goodenough, J.B.; Shao-Horn, Y. A Perovskite Oxide Optimized for Oxygen Evolution Catalysis from Molecular Orbital Principles. *Science* **2011**, *334*, 1383–1385. [CrossRef]
36. Xu, X.; Pan, Y.; Zhong, Y.; Ran, R.; Shao, Z. Ruddlesden–Popper perovskites in electrocatalysis. *Mater. Horiz.* **2020**, *7*, 2519. [CrossRef]
37. Malkhandi, S.; Trinh, P.; Manohar, A.K.; Manivannan, A.; Balasubramanian, M.; Prakash, G.K.S.; Narayanan, S.R. Design Insights for Tuning the Electrocatalytic Activity of Perovskite Oxides for the Oxygen Evolution Reaction. *J. Phys. Chem. C* **2015**, *119*, 8004–8013. [CrossRef]
38. Tanaka, H.; Misono, M. Advances in Designing Perovskite Catalysts. *Curr. Opin. Solid State Mater. Sci.* **2001**, *5*, 381–387. [CrossRef]
39. Harris, J. Low-Cost Oxygen Electrode Material, The Flow of Non-Newtonian Fluids under a Varying Pressure Gradient. *Nature* **1970**, *226*, 848–849. [CrossRef]
40. Ghanem, M.A.; Amer, M.S.; Al-Mayouf, A.M.; Arunachalam, P.; Weller, M.T. Halide-Doping Effect of Strontium Cobalt Oxide Electrocatalyst and the Induced Activity for Oxygen Evolution in an Alkaline Solution. *Catalysts* **2021**, *11*, 1408. [CrossRef]
41. Gao, W.; Wang, C.; Ma, F.; Wen, D. Highly active electrocatalysts of CeO_2 modified $NiMoO_4$ nanosheet arrays towards water and urea oxidation reactions. *Electrochim. Acta* **2019**, *320*, 134608. [CrossRef]
42. Yu, Z.-Y.; Lang, C.-C.; Gao, M.-R.; Chen, Y.; Fu, Q.-Q.; Duan, Y.; Yu, S.-H. Ni−Mo−O nanorod-derived composite catalysts for efficient alkaline water-to-hydrogen conversion via urea electrolysis. *Energy Environ. Sci.* **2018**, *11*, 1890–1897. [CrossRef]
43. Galal, A.; Atta, N.F.; Hefnawy, M.A. Voltammetry study of electrocatalytic activity of lanthanum nickel perovskite nanoclusters-based composite catalyst for effective oxidation of urea in alkaline medium. *Synth. Met.* **2020**, *266*, 116372. [CrossRef]
44. Yang, D.; Yang, L.; Zhong, L.; Yu, X.; Feng, L. Urea electrooxidation efficiently catalyzed by nickel-molybdenum oxide nanorods. *Electrochim. Acta* **2019**, *295*, 524–531. [CrossRef]

45. Mefford, J.T.; Hardin, W.G.; Alexander, C.T.; Johnston, K.P.; Stevenson, K.J. Nanostructured $LaNiO_3$ Perovskite Electrocatalyst for Enhanced Urea Oxidation. *ACS Catal.* **2016**, *6*, 5044–5051. [CrossRef]
46. Hagenmuller, P. *Inorganic Solid Fluorides Chemistry and Physics*; Academic Press: New York, NY, USA, 1985.
47. Kim, S.W.; Kim, S.-H.; Halasyamani, P.S.; Green, M.A.; Bhatti, K.P.; Leighton, C.; Dase, H.; Fennie, C.J. $RbFe^{2+}Fe^{3+}F_6$: Synthesis, structure, and characterization of a new charge ordered magnetically frustrated pyrochlore-related mixed-metal fluoride. *Chem. Sci.* **2012**, *3*, 741–751. [CrossRef]
48. Weller, M.T.; Hughes, R.W.; Rooke, J.; Kneea, C.S.; Reading, J. The pyrochlore family: A potential panacea for the frustrated perovskite chemist. *Dalton Trans.* **2004**, *2004*, 3032–3041. [CrossRef]
49. Lemoine, K.; Lhoste, J.; Hémon-Ribaud, A.; Heidary, N.; Maisonneuve, V.; Guiet, A.; Kornienko, N. Investigation of mixed-metal (oxy) fluorides as a new class of water oxidation electrocatalysts. *Chem. Sci.* **2019**, *10*, 9209–9218. [CrossRef]
50. Li, M.; Liu, H.; Feng, L. Fluoridation-induced high-performance catalysts for the oxygen evolution reaction: A mini review. *Electrochem. Commun.* **2021**, *122*, 10690. [CrossRef]
51. Zhang, H.; Guan, D.; Gu, Y.; Xu, H.; Wang, C.; Shao, Z.; Guo, Y. Tuning synergy between nickel and iron in Ruddlesden–Popper perovskites through controllable crystal dimensionalities towards enhanced oxygen-evolving activity and stability. *Carbon Energy* **2024**, e465. [CrossRef]
52. Tang, J.; Xu, X.; Tang, T.; Zhong, Y.; Shao, Z. Perovskite-Based Electrocatalysts for Cost-Effective Ultrahigh-Current-Density Water Splitting in Anion Exchange Membrane Electrolyzer Cell. *Small Methods* **2022**, *6*, 2201099. [CrossRef] [PubMed]
53. Aladeemy, S.A.; Al-Mayouf, A.M.; Amer, M.S.; Alotaibia, N.H.; Weller, M.T.; Ghanem, M.A. Structure and electrochemical activity of nickel aluminium fluoride nanosheets during urea electro-oxidation in an alkaline solution. *RSC Adv.* **2021**, *11*, 3190–3201. [CrossRef] [PubMed]
54. Masachchi, L.W.; Keerthisinghe, N.; Morrison, G.; Berseneva, A.A.; Smith, M.D.; zur Loye, H.-C. Crystal Growth and Magnetism of Transition Metal Pyrochlore Fluorides. *Inorg. Chem.* **2023**, *62*, 13793–13801. [CrossRef] [PubMed]
55. Cheek, G.T.; O'Grady, W.E. Redox behavior of the nickel oxide electrode system: Quartz crystal microbalance studies. *J. Electroanal. Chem.* **1997**, *421*, 173–177. [CrossRef]
56. Wang, D.; Liu, S.; Gan, Q.; Tian, J.; Isimjan, T.T.; Yang, X. Two-dimensional nickel hydroxide nanosheets with high content of nickel(III) species towards superior urea electro-oxidation. *Electroanal. Chem.* **2018**, *829*, 81. [CrossRef]
57. Gan, Q.; Cheng, X.; Chen, J.; Wang, D.; Wang, B.; Tain, J.; Isimjan, T.; Yang, X. Temperature effect on crystallinity and chemical states of nickel hydroxide as alternative superior catalyst for urea electrooxidation. *Electrochim. Acta* **2019**, *301*, 47. [CrossRef]
58. Wu, M.S.; Lin, G.W.; Yang, R.S. Hydrothermal growth of vertically aligned ordered mesoporous nickel oxide nanosheets on three-dimensional nickel framework for electrocatalytic oxidation of urea in alkaline medium. *J. Power Sources* **2014**, *272*, 711. [CrossRef]